J Solid State Electrochem (2009) 13:1241–1250
DOI 10.1007/s10008-008-0653-9

ORIGINAL PAPER

The $NiFe_2O_4 - MgFe_2O_4$ series as electrode materials for electrochemical reduction of NO_x

F. Bræstrup · K. K. Hansen

Received: 16 May 2008 / Revised: 12 August 2008 / Accepted: 12 August 2008 / Published online: 5 September 2008

Abstract Solid solutions of spinel-type oxides with the composition $Ni_{1-x}Mg_xFe_2O_4$ ($x = 0.0, 0.3, 0.5, 0.6, 1.0$) were prepared with the glycine-nitrate combustion synthesis ($x = 0.0, 0.3, 0.5, 0.6$) and the citric-acid combustion synthesis ($x = 1.0$). The oxides were used as electrode materials in a pseudo-three-electrode setup in the temperature range of 400–600 °*C*. Cyclic voltammetry and electrochemical impedance spectroscopy were used to characterize the electrochemical behavior in 1% NO and 10% O_2. Measurements show that $NiFe_2O_4$ has relatively high cathodic activity in both NO and O_2, whereas $MgFe_2O_4$ shows much higher activity in NO compared to O_2. $MgFe_2O_4$ was also measured with cyclic voltammetry in 1% NO_2 and different gas mixtures of NO and O_2 at 300 and 400 °C. Results show that the cathodic activities (−0.6 V) are relatively high with current ratios, $I_{NO_x+O_2}/I_{O_2}$, ranging from 10.1–167.7 and with a maximum at 400 °C. Dilatometry measurements were performed on the materials in air up to 1,000 °C, and they showed that the Curie temperature could be detected for all samples. Four-point DC resistivity measurements at elevated temperatures show that $Ni_{0.4}Mg_{0.6}Fe_2O_4$ has the highest conductivity, whereas $Ni_{0.7}Mg_{0.3}Fe_2O_4$ and $NiFe_2O_4$ have the highest conductivity at lower temperatures.

Keywords Spinel-type oxide · Conductivity · Powder diffraction · NO_x · O_2

F. Bræstrup (✉) · K. K. Hansen
Fuel Cells and Solid State Chemistry Department,
Risø National Laboratory for Sustainable Energy,
Technical University of Denmark, Copenhagen, Denmark
e-mail: frantz.braestrup@risoe.dk

Introduction

One of the main polluting agents from internal combustion processes in diesel-fired engines is NO_x (NO and NO_2) gases. Presently, the three-way catalytic converter (TWCC) is employed for treating gasoline engine emissions; however, the TWCC requires stoichiometric conditions to simultaneously catalyze oxidizing and reducing reactions. This makes it unsuitable in lean burn and diesel engine applications. Several attempts have been made to solve the problem with NO_x emission, and the one that has gained the most attention is the system based on the selective catalytic reduction process (SCR). In SCR, the reduction of NO_x is performed by injecting a reducing agent, such as ammonia, urea, or a hydrocarbon into the exhaust gas upstream of the SCR catalyst. Although the SCR technology has been shown to reduce NO_x by 65–99% [1] over a range of diesel operating conditions, one of the disadvantages with mobile SCR technology is that the reduction agent must be carried onboard in a tank, which places some requirements on packing the substance. It also has to be durable and function-effective in a diverse range of a truck engines. Moreover, systems must be designed to prevent unreacted reducing agents to escape out of the tailpipe of the vehicle, as well as N_2O formation.

An alternative route is to reduce NO_x electrochemically in an all solid-state reactors [2]. The NO_x gases are reduced at the cathode following the overall Eqs. 1 and 2:

$$4e^- + 2NO \rightarrow N_2 + 2O^{2-} \quad (1)$$

$$4e^- + NO_2 \rightarrow 0.5N_2 + 2O^{2-}. \quad (2)$$

A drawback is that O_2 can also be reduced at the cathode (Eq. 3), which will lead to a high consumption of current.

$$4e^- + O_2 \rightarrow 2O^{2-}. \quad (3)$$

A good electrode material therefore has to be selective towards reduction of NO and NO_2, as well as a good electronic conductor and/or a good ion conductor. Since NO and NO_2 are less stable than O_2, the energy level of the antibonding orbitals of NO_x is located at a lower energy level than the corresponding antibonding orbitals of O_2. By adjusting the potential in such a way that the valence electrons of the electrode material are placed at an energy level in between that of the antibonding orbitals of NO (or NO_2) and O_2, it will be possible to reduce only the NO_x [3].

Previous reports using metal electrodes such as Pd, Pt, Au, Ag, Ir, and NiO [2, 4–9] on an yttrium stabilized zirconia (YSZ) oxygen ion conductor have shown some interesting results; however, most of the metals are relatively expensive, which has intensified the research for low-cost ceramics to be used as electrode materials. RuO_2 has also been suggested as a candidate for electrochemical NO_x removal [5]; however, Ru is highly poisonous and forms higher volatile oxides, such as RuO_3 and RuO_4. Catalytic NO_x decomposition on spinel-type oxides [10–14] has been reported; however, only a few observations on electrochemical decomposition on spinel-type electrode materials [15, 16] have been presented in literature to our knowledge. In this study, the electrochemical reduction of NO_x and O_2 has been investigated on point electrodes of spinel-type oxides, $Ni_{1-x}Mg_xFe_2O_4$ ($x = 0.0, 0.3, 0.5, 0.6, 1.0$), with the purpose of finding cheap electrode materials, of nonprecious metals, to be used in electrochemical filters placed on diesel-fired vehicles.

Experimental details

Sample preparation and X-ray diffraction

$Ni_{1-x}Mg_xFe_2O_4$ ($x = 0.0, 0.3, 0.5, 0.6, 1.0$) were prepared from aqueous metal nitrates ($Ni(NO_3)_2 \cdot 2.6\ H_2O$, $Mg(NO_3)_2 \cdot 2.6\ H_2O$, and $Fe(NO_3)_2 \cdot 3.9\ H_2O$) using the glycine-nitrate combustion synthesis [17] ($x = 0.0, 0.3, 0.5, 0.6$) and the citric-acid combustion synthesis [18] ($x = 1.0$). After synthesis, the powder was ball-milled for 24 h and then calcined in air at 1,000 °C for 6 h. All samples were analyzed by X-ray diffraction using a STOE theta-theta diffractometer. Scans were conducted over the 2θ-range of $15° - 80°$, with a step width of 0.05°. Le Bail fits were carried out using the program Jana2000 [19] in order to determine the unit cell parameter, **a**. Pseudo-Voigt profile functions were used, and the background was modeled with 10-term Legendre polynomials.

The powder was pressed uniaxially at 1 ton into elongated pellets, followed by isostatic pressing at 50 tons to make the pellets more dense and to increase their mechanical strength. The samples were then sintered in air at 1,000 °C for 6 h. The pellets were then mechanically tooled into cone-shaped electrodes as described by others [20, 21].

Cyclic voltammetry and impedance spectroscopy

Cyclic voltammetry (CV) and electrochemical impedance spectroscopy (EIS) were recorded with a Gamry Femtostate in a pseudo-three-electrode setup [22] suggested by Fabry [23]. The cone, acting as a point electrode, was arranged with the tip placed downwards on a polished one-end closed YSZ-tube electrolyte containing air as reference gas and a silver electrode used as the counter/reference electrode. CV and EIS were recorded at 400, 500, and 600 °C in 10% O_2 in Ar or 1% NO in Ar (Air Liquide) with a flow rate of 20 ml/min. Additional measurements were performed on the $MgFe_2O_4$-electrode in 1 % NO_2 in Ar and gas mixtures of 0.5% NO + 5% O_2, 0.5% NO + 10% O_2, and 0.5% NO_2 + 10% O_2. Measurements containing NO_2 gas (Air Liquide) were performed only at 300 and 400 °C. A 1-h equilibrium time was used to record the open current voltage (OCV) before recording the voltammograms in the potentional range of -0.6 V $- 0.5$ V with a sweep rate of 1.0 and 10 mV s^{-1}. EIS were recorded from 177,793(1) to 0.050(1) Hz with 10 points/decade and an amplitude of 24 mV (rms). In order to compare the electrodes directly, the currents in the voltammograms were converted to current densities by dividing with the contact area, which was determined by EIS using Newman's formula [24], Eq. 4,

$$r = \frac{1}{4\sigma R_e}. \quad (4)$$

Newmann's formula assumes that the contact area is circular, with r being the radius of the contact area, σ is the specific conductivity of the electrolyte material and R_e is the electrolyte resistance. σ can be determined from Eq. 5 [25].

$$\sigma = \frac{1.51 \cdot 10^6}{T} \cdot e^{\frac{-0.94[eV]}{Tk_B}} \quad (5)$$

where T and k_B are the temperature and the Boltzman's constant, respectively.

Dilatometry and thermogravimetry

The linear thermal expansion was measured by dilatometry in air (flow rate: 50 ml/min) using a NETZSCH DIL 402C dilatometer with a sample load of 30.000 cN. The sample-rod was heated from room temperature up to 1,000 °C and back at 2 °C/min. The sample remained at 1,000 °C for 2 h. Data were calibrated to an Al_2O_3 standard at identical conditions. Thermogravimetry (TG) measurements on (~ 46 mg) $MgFe_2O_4$ were performed on a NETZSCH TG 439 thermo microbalance in air (flow rate: 50 ml/min). The measurement was run with the same temperature profile as used in the dilatometry measurements.

Four-point DC resistivity measurements

Platinum paste was applied to each end of the elongated rod and contacted with platinum leads. Two platinum potential probes with a fixed distance were positioned on one side of the bar. The data collection was made with an in-house data acquisition software, ELCHEMEA. The resistivity was measured every 5 min from room temperature to 1,000 °C and back again with a ramp rate of 2 °C/min and a 2-h dwell at every 50-°C interval. The resistivities of the samples were corrected for the porosity using the Bruggerman asymmetric model [26]. The densities of the elongated rods were measured by the Archimedes principle. Measurements showing signs of sintering were repeated in order to minimize its effects.

Results and discussions

Almost all materials were single-phase spinel-type oxides. However, a small impurity phase of NiO (approx. 1%) was observed in $Ni_{0.5}Mg_{0.5}Fe_2O_4$. X-ray diffraction measured at room temperature showed an increase in unit cell parameters with increasing Mg content (Fig. 1). $NiFe_2O_4$ has an inverse spinel-type structure with Ni^{2+} located primarily on the octahedral sites and Fe^{3+} located on both the tetrahedral and the octahedral sites. The ionic radii of Ni^{2+} on a tetrahedral and an octahedral site are 0.55 Å and 0.69 Å respectively, whereas Fe^{3+} has an ionic radius of 0.63 Å (tetrahedral sites) or 0.65 Å(octahedral sites) [27]. When Mg^{2+}, having an ionic radius of 0.57 Å (tetrahedral sites) or 0.72 Å (octahedral sites) is introduced in the structure in favor of Ni^{2+}, it will enter the tetrahedral lattice site, therefore forcing Fe^{3+} on the tetrahedral site to move into an octahedral site. That would, in principle, not increase the volume of the unit cell. However, although

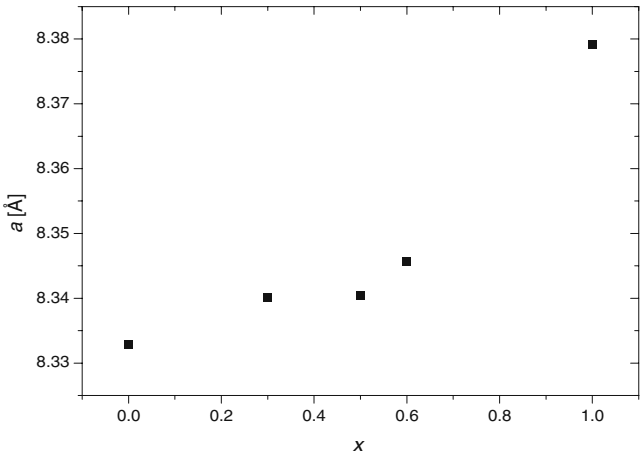

Fig. 1 Unit cell parameters, *a*, at different spinel compositions. A small increase in *a* is observed from $0.0 \leq x \leq 0.6$, whereas the unit cell is significantly higher at $x = 1.0$. *Error bars* are at the same magnitude as the dimension of the points

the increase in unit cell is very small in the range of $0 \leq x \leq 0.6$, some of the Mg^{2+} must be located on the octahedral sites, otherwise, there will be no expansion of the unit cell. This is due to the fact that Mg^{2+} is 11% bigger than Fe^{3+} on an octahedral site. The relatively large unit cell expansion of $MgFe_2O_4$ is a result of the structure now favoring a pseudoinverse spinel-type structure [28] with Mg^{2+} located mainly on octahedral sites and Fe^{3+} on tetrahedral and octahedral sites. The solid solution of $NiFe_2O_4$ and $MgFe_2O_4$ therefore covers the change from an inverse spinel-type structure towards a more normal spinel-type structure and back to a pseudoinverse spinel-type structure.

Conductivity measurements

Figure 2 shows the specific conductivity of the spinels as a function of temperature. A large hysteresis is only observed for $Ni_{0.7}Mg_{0.3}Fe_2O_4$. At high temperatures (above ~ 700 °C), the conductivity increases as more Mg is substituted with Ni (maximum at $x = 0.5$). At higher Mg content, the conductivity decreases again, as also described in earlier reports [29, 30]. However, they found a maximum conductivity for $Ni_{0.4}Mg_{0.6}Fe_2O_4$. The conductivity is mainly attributed to the cation–anion–cation super exchange interactions between octahedral sites, where the transport property rises from hopping of localized *d* electrons between cations on octahedral sites [31, 32]. Mg^{2+} will, as discussed in the "Results and discussions" section, enter the tetrahedral sites, resulting in a migration of Fe^{3+} ions into the octahedral sites. The increase in concentration of

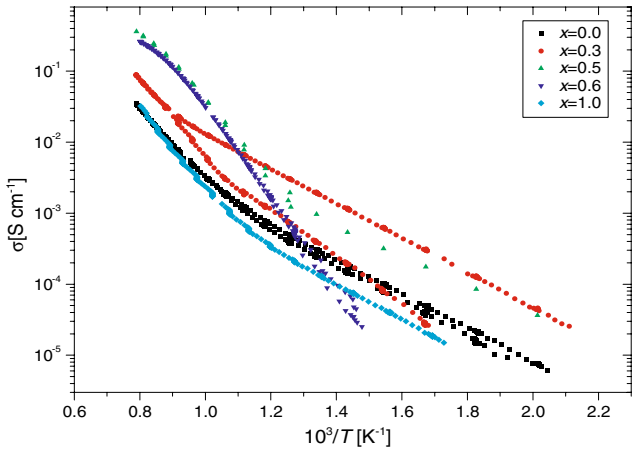

Fig. 2 Four-point DC conductivity measurements of the spinels measured from room temperature to 1,000 °C in air

Fe^{3+} on the octahedral sites will increase the hopping rate of the electrons. Increasing the Mg^{2+} content will eventually force the Mg^{2+} ions to occupy the octahedral sites, leaving the Fe^{3+} ions to migrate back onto the tetrahedral sites. This will lower the concentration of Fe^{3+} ions on the octahedral sites and, therefore, also the hopping rate of the electrons. The data were fitted with an Arrhenius Eq. 6,

$$\sigma = \sigma_0 \exp \frac{-E_a}{k_B T}, \tag{6}$$

where σ is the specific conductivity and E_a is the activation energy.

The conductivities of $NiFe_2O_4$ and $MgFe_2O_4$ behave in a similar way. Both show a slightly curved behavior starting at 607 °C ($NiFe_2O_4$) and 574 °C ($MgFe_2O_4$). $NiFe_2O_4$ has a Curie point in the range of 585–590 °*C* [33, 34], which could explain some of the changes in conductivity. However, the change in conductivity of $NiFe_2O_4$ and $MgFe_2O_4$ is more likely a result of reordering of the cations (see the "Dilatometry" section). Activation energies (Table 1) are very similar for $NiFe_2O_4$ and $MgFe_2O_4$. At lower temperatures, activation energies are in the range of 0.415–0.536 eV, with $MgFe_2O_4$ having the highest activation energies. At high temperatures, activation energies decrease to 0.177–0.214 eV.

The conductivity of $Ni_{1-x}Mg_xFe_2O_4$, $(x = 0.5, 0.6)$ shows a more different behavior. The conductivity increases quite rapidly from 500 to 800 °C compared to the other samples. Above 800 °C, the conductivity changes slope towards a lower activation energy. This more metallic behavior is a result of a direct cation–cation interaction on octahedral sites also observed in Cu-containing ferrite with a spinel-type structure [31, 32]. $Ni_{0.5}Mg_{0.5}Fe_2O_4$ shows a significant change in conductivity at 495 °C, which might be related to the Curie temperature.

During heating, $Ni_{0.7}Mg_{0.3}Fe_2O_4$ follows the same trend as both $NiFe_2O_4$ and $MgFe_2O_4$, but the conductivity during cooling is significantly higher. The large hysteresis of $Ni_{0.7}Mg_{0.3}Fe_2O_4$ must be a result of the changes in the cation distribution. The upward curvature of the conductivity takes place at higher temperatures than that of both $NiFe_2O_4$ and $MgFe_2O_4$. When the sample is cooled below the critical temperature (blocking temperature), a relatively large amount of Mg^{2+} is trapped in the tetrahedral sites. This will leave the Fe^{3+} and the Ni^{2+} on the octahedral sites and thereby increase the conductivity relative to the heating stage.

Dilatometry

Earlier reports show that spinels in general are bad oxygen ion conductors. A composite electrode of spinel and $Ce_{0.9}Gd_{0.1}O_{1.95}$ (CGO10) (an oxygen ion conductor, which has a higher ionic conductivity than YSZ at low temperatures) are therefore needed in order to have a proper current running. It is therefore important to know the thermal expansion coefficient of the spinels when it is mixed with other materials.

Measurements with dilatometry show, with an exception of $MgFe_2O_4$, a single discontinuity of the relative linear expansion (see Fig. 3). This is observed during both the heating and cooling stages and is

Table 1 Activation energies, E_a, calculated from the conductivity measurements

Compound	E_a, high T, H	E_a, high T, C	E_a, low T, H	E_a, low T, C
$NiFe_2O_4$	0.211(1) eV	0.207(1) eV	0.415(1) eV	0.449(1) eV
$Ni_{0.7}Mg_{0.3}Fe_2O_4$	0.286(1) eV	0.209(1) eV	0.471(2) eV	0.416(2) eV
$Ni_{0.5}Mg_{0.5}Fe_2O_4$	–	0.179(4) eV	0.489(2) eV	0.448(6) eV
$Ni_{0.4}Mg_{0.6}Fe_2O_4$	–	–	0.287(1) eV	0.298(2) eV
$MgFe_2O_4$	0.177(1) eV	0.214(1) eV	0.536(4) eV	0.477(3) eV

H and C represent the heating and the cooling stages. T is the temperature. Estimated standard deviations are in parentheses.

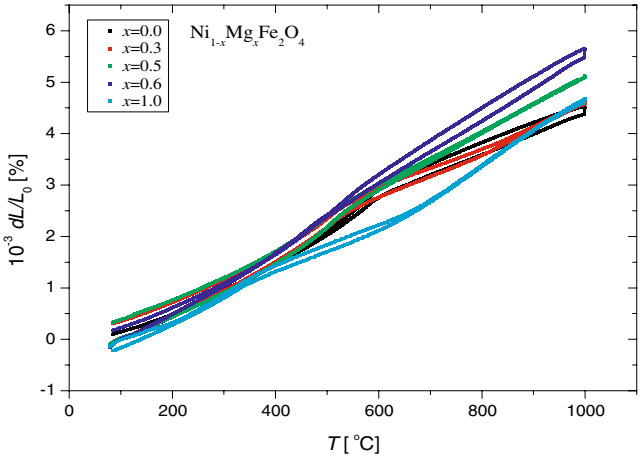

Fig. 3 Linear expansion of the different spinels measured in the temperature range of 80 to 1,000 °C. The Curie point is detectable for all of the spinels

related to the Curie temperature, T_c [33]. The thermal expansion coefficient, α, defined as $\alpha = \frac{1}{L}\frac{\delta L}{\delta T}$, does not change much before or after T_c, although it reaches a slightly lower value after T_c (see Table 2).

In general, T_c measured during cool down is located at slightly lower temperatures compared to the heating stage (see Table 2). T_c also decreases with increasing Mg content of the Ni-containing spinels. Figure 4 shows the dilatometry measurements of $MgFe_2O_4$. The relative linear expansion reveals two discontinuities at 327 and 800 °C, both appearing during the heating and the cooling stages. α shows a sharp peak at 325 °C as in the case of the Ni-containing materials, whereas the peak at 800 °C is much more broad (starts appearing at 620 °C (heating) or 570 °C (cooling)). The first discontinuity is related to the magnetic ordering of the Fe electrons, although there seem to be some disagreements on the type of magnetic ordering [35–37]. The T_c peak was not observed by Carter [38] and Weil [39], who concluded that the magnetic exchange interaction energy is independent of the Fe–O–Fe spacing. Our results, however, show that this is not the case. In $MgFe_2O_4$, T_c is highly sensible to the cation distribution [35], which again is very sensible to the thermal history of the spinel. The reason for the different results must be found in the difference in sample preparation (more Fe^{3+} on octahedral sites will increase the number of super exchange interactions and make the Curie point more pronounced) or the number of collected data points. Carter narrowed his data set down to ~ 20 data points, which makes it difficult to detect a relatively narrow peak if present.

The second discontinuity, starting at 620 °C, is more difficult to explain but seems to be related to some sort of structural expansion superimposed onto the thermal expansion. Carter also detected the same kind of upward curvature of the expansion of $MgFe_2O_4$ but was not able to explain the phenomena. One origin of the structural expansion would be a change of stoichiometry (loss of oxygen). This would result in a structural expansion as also reported for different oxides [40, 41]. However, TG measurements show no sign of oxygen loss at the specific temperature. Another explanation would be to relate the upward curvature of the expansion to the order–disorder transition between cations on tetrahedral and octahedral sites. Discussed in the "Results and discussions" section is the ionic radius of the cations responsible for the change of the lattice parameters. In most cases, the compounds are not in equilibrium at low temperatures, where the orderings of the cations are controlled by the kinetics [42]. At high temperatures, the spinels are in equilibrium with respect to the cation order–disorder, reflecting the thermodynamic drive towards high-temperature disorder. The increase of the relative linear expansion at 620 °C results from the starting value of the ordering parameter being lower than the equilibrium value. When the interaction between kinetics and thermodynamics allows it, Mg^{2+} will start to jump to an octahedral site and thereby force the unit cell to expand faster than the thermal vibrations allow. At around 800 °C, the cation order–disorder has reached an equilibrium leading the thermal expansion to take over the main process and thereby decreasing the relative linear expansion. Earlier reports [35, 43] show that the ordering of the cations at equilibrium temperatures starts somewhere between 400 and 650 °C, which is in good

Table 2 Curie temperatures, T_c, and expansion coefficients, α

Compound	T_c (heating)	T_c (cooling)	$\alpha_{400\,°C}$	$\alpha_{800\,°C}$
$NiFe_2O_4$	584 °C	581 °C	$1.13 \cdot 10^{-5}$	$8.08 \cdot 10^{-6}$
$Ni_{0.7}Mg_{0.3}Fe_2O_4$	516 °C	510 °C	$1.30 \cdot 10^{-5}$	$1.26 \cdot 10^{-5}$
$Ni_{0.5}Mg_{0.5}Fe_2O_4$	510 °C	499 °C	$1.20 \cdot 10^{-5}$	$1.10 \cdot 10^{-5}$
$Ni_{0.4}Mg_{0.6}Fe_2O_4$	468 °C	466 °C	$1.16 \cdot 10^{-5}$	$7.75 \cdot 10^{-6}$
$MgFe_2O_4$	327 °C	325 °C	$^{*}6.17 \cdot 10^{-5}$	$7.38 \cdot 10^{-4}$

The α value, marked with *, is measured at 500 °C.

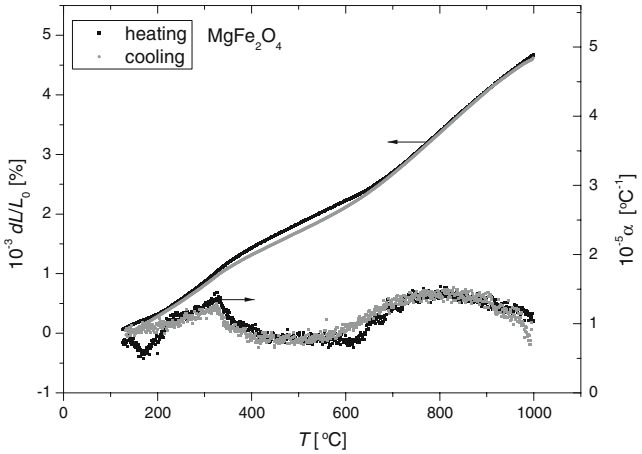

Fig. 4 Linear expansion and expansion coefficients of $MgFe_2O_4$. The peak at ~ 325 °C is the Curie temperature, T_c and the broad peak at 800 °C is due to cation ordering

agreement with our results. The structural expansion takes place over a range of ~ 180 °C, which is also similar to what is reported by Harrison. Antao [44] measured the cation ordering in $MgFe_2O_4$ using in situ, high-temperature synchrotron X-ray powder diffraction. They found that, when heating the sample, the cations start to jump between lattice sites at 581 °C (more Mg^{2+} on octahedral sites), and during cooling, the cations jump back to their original position until the blocking temperature is reached at 543 °C. This will explain not only the change of conductivity in the same temperature range but also the behavior of the linear expansion in our experiments.

A small uptake of oxygen at 985 °C was detected with TG. Thermodynamic calculations (FactSage [45]) show that $MgFe_2O_4$ will decompose to MgO and a more Fe-rich spinel at 980 °C. $MgFe_2O_4$ have been found to be slightly over-stoichiometric with respect to the metal ions [46], which will explain the small uptake of oxygen following reaction 7:

$$\delta O_2 + MgFe_2O_{4-\delta} \rightarrow \delta MgO + Mg_{1-\delta}Fe_2O_4. \qquad (7)$$

The phase change was not observed in the dilatometry measurements because of slow kinetics [47]. However, a small amount of the material has decomposed during the experiment, which was confirmed in the TG measurement. The expansion coefficients of the spinels ($\alpha = 10 \cdot 10^{-6} - 15 \cdot 10^{-6}$ °C^{-1}) are very similar to the expansion coefficient of CGO10 ($\alpha = 11.9 \cdot 10^{-6}$ °C^{-1} [48]), so a composite electrode of our spinels and CGO10 seems possible.

Cyclic voltammetry

Figure 5 shows the voltammogram recorded at 400 °C. Similar voltammograms were also recorded at 500 and 600 °C; however, they look very similar to those recorded at 400 °C and are therefore not shown for all of the spinels. Part of the voltammograms recorded on $NiFe_2O_4$ and $MgFe_2O_4$ are shown in Fig. 6 since they show a more interesting behavior than that of the rest of the spinels. $NiFe_2O_4$ has the highest cathodic activity in NO and O_2 at 500 and 600 °C. However, at 400 °C, $MgFe_2O_4$ shows higher activity in NO than $NiFe_2O_4$ does. The activity in O_2 differs significantly between the two electrode materials, with $NiFe_2O_4$ showing the highest activity. Figure 7 shows the current densities in NO and O_2 as a function of the Mg^{2+} content. As more Mg^{2+} is substituted into the $NiFe_2O_4$ compound, the activity in NO and O_2 decreases significant until a minimum is reached at the $Ni_{0.5}Mg_{0.5}Fe_2O_4$ electrode. The activity on $Ni_{0.4}Mg_{0.6}Fe_2O_4$ increases slightly again, but on the $MgFe_2O_4$, electrode the picture looks more blurry. Figure 8 shows the current ratios of NO with respect to O_2. Ni-containing electrode materials all show current ratios in the range of 0.4–2.4 but without any systematic trends. It was not possible for us to reproduce the measurements from Simonsen [15], who got some very interesting results on $NiFe_2O_4$ (potential range −1.0–0.5 V). However, theoretically, electrochemical calculations [45] show that $NiFe_2O_4$ is reduced to Ni + Fe_3O_4 at potentials lower than −0.86 V (600 °C). In our measurements, we did not go below −0.6 V at any temperature, which might explain why our measurements did not match

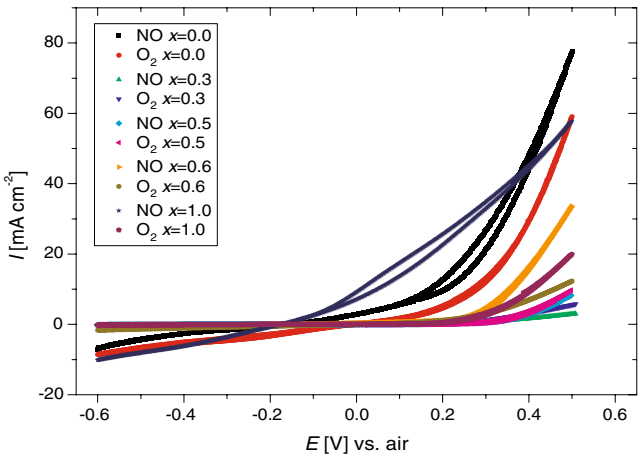

Fig. 5 Cyclic voltammograms on the different spinels at 400 °C. Data were recorded in 1% NO and in 10% O_2 with air as reference gas (sweep rate: 1 mV/s)

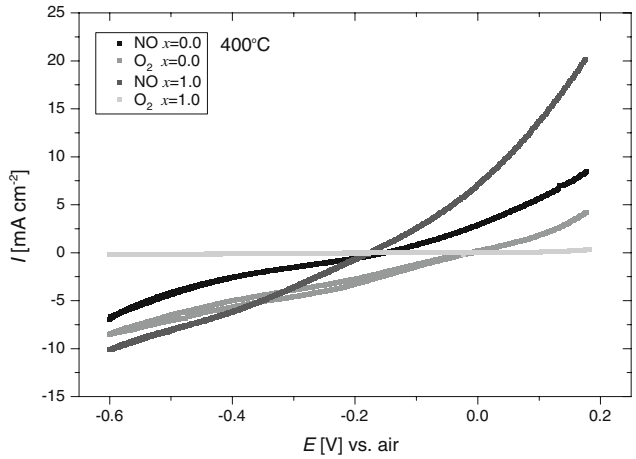

(a)

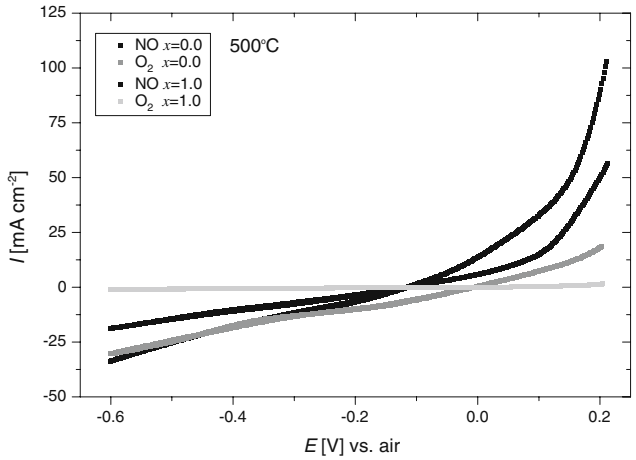

(b)

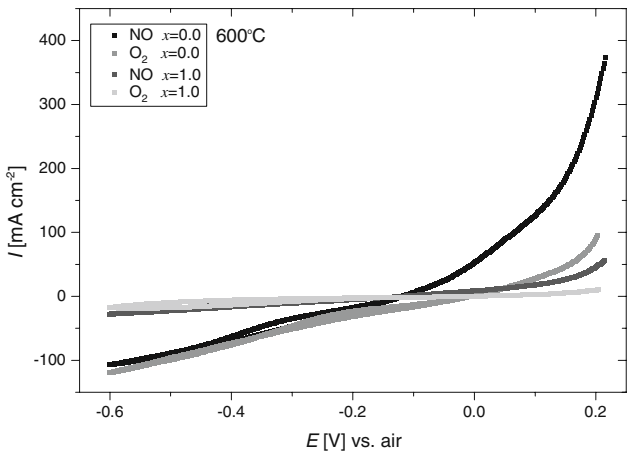

(c)

Fig. 6 Cyclic voltammogram on $NiFe_2O_4$ and $MgFe_2O_4$. **a**, **b**, and **c** show a part of the voltammograms (−0.6–0.2 V) at 400, 500, and 600 °C, respectively. The voltammograms were recorded in 1% NO and in 10% O_2 with air as reference gas (sweep rate: 1 mV/s)

theirs. A comparison of our results with Hansen [16] is more difficult. Their data have not been normalized to current densities and the NO concentration used

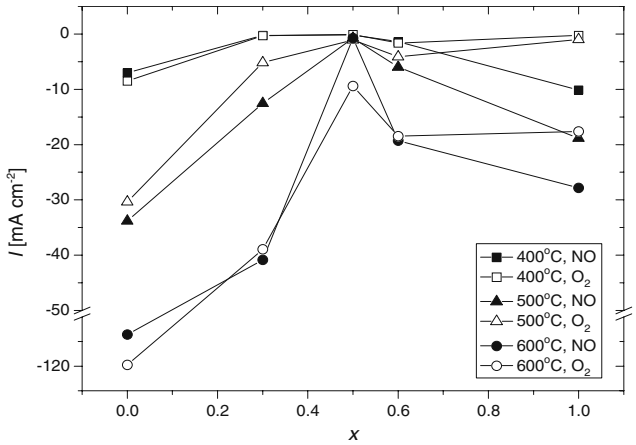

Fig. 7 Current densities in NO and O_2 using the different electrode materials ($Ni_{1-x}Mg_xFe_2O_4$). Data are shown for 400, 500, and 600 °C. *x* refers to the Mg content

is twice as high as in our measurements. However, estimated values of the current ratios are much smaller ($(I_{NO}/I_{O_2} \leq 1)$ than we find, which makes our materials more interesting.

The activities of the spinels seem to be correlated to the distribution of Fe^{3+} on different lattice sites. The more Fe^{3+} is located on the tetrahedral sites, the more active is the spinel. $NiFe_2O_4$ has the highest content of Fe^{3+} on tetrahedral sites among the spinels, and it also has the highest activity. As more Mg^{2+} is incorporated into the lattice, the more Fe^{3+} will be located on octahedral sites, causing an increase in conductivity (in air) and a decrease in activity. When the Mg^{2+} content reaches a critical value ($x = 0.5$), the structure now

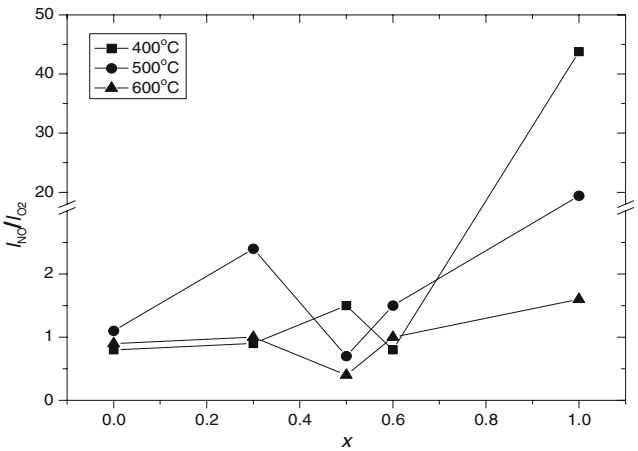

Fig. 8 Current ratios between NO and O_2 for the different spinels ($Ni_{1-x}Mg_xFe_2O_4$). $MgFe_2O_4$ shows significantly higher current ratios at 400 and 500 °C compared to the other spinels. *x* refers to the Mg content

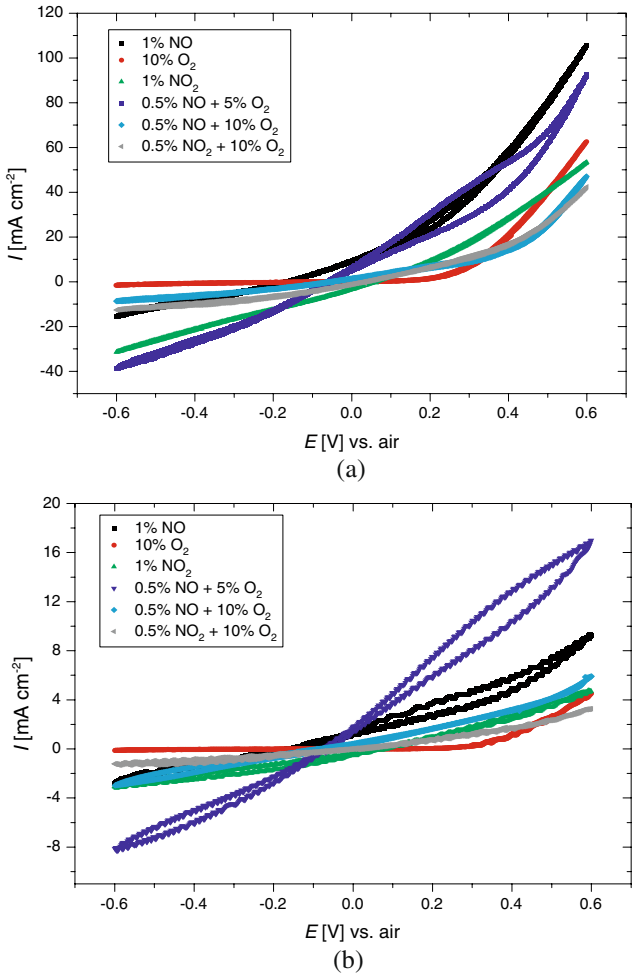

Fig. 9 Cyclic voltammograms on $MgFe_2O_4$ in different gas mixtures at 400 °C (**a**) and 300 °C (**b**). Air was used as reference gas and data were collected with a sweep rate of 1 mV/s. The electronic noise at 300 °C is notable

favors Mg^{2+} to move to octahedral sites and Fe^{3+} to tetrahedral sites. This causes a decrease in conductivity and an increase in activity. If Ni^{2+} had the dominant effect on the activity, we would expect a decrease in activity with increasing Ni^{2+} content, but we will be left to explain the high activity on $MgFe_2O_4$. If Mg^{2+}, on the other hand, had the dominant effect on the activity, we would expect an increase in activity with increasing Mg^{2+} content.

In general, $MgFe_2O_4$ shows higher activity in NO than in O_2 at all temperatures, with a maximum current ratio at 400 °C. Additional measurements in 1% NO_2 and different gas mixtures (0.5% NO_2 + 5% O_2, 0.5% NO_2 + 10% O_2, 0.5% NO + 10% O_2) were therefore performed on the $MgFe_2O_4$ electrode material in the temperature range of 300–600 °C. Figure 9a and b show the voltammogram at 400 and 300 °C, respectively. Measurements at 300 °C show that activity in NO at −0.6 V is higher than in O_2. The activity in NO_2 and 0.5 % NO + 5 % O_2 is higher than both NO and O_2. The much higher activity in 0.5 % NO + 5 % O_2 is presumably influenced by the fact that a small concentration of NO_2 is formed in the gas mixture; however, other reaction mechanisms/processes not identified seem to dominate the system. The presence of 5% O_2 together with NO does not seem to block the active sites, otherwise the activity would has been somewhere lower. Higher oxygen partial pressure seems to inhibit the reduction of NO quite substantially.

Figure 10 shows the current ratios with respect to O_2 at −0.6 V as a function of temperature. In the case of NO and NO + O_2, the current ratios peak at 400 °C with maximums of 43.8 and 167.7, respectively. Measurements in NO_2 and NO_2 + O_2 at 300 and 400 °C show maximum current ratios of 135.9 and 54.8, respectively. No measurements were made at lower temperatures because of the relatively low electronic conductivity of $MgFe_2O_4$. The ratios of the current densities peak at 400 °C and then fall off almost symmetrically around the peak. Measurements in O_2 + NO_2 and in NO_2 were only made at two different temperatures, so we can therefore not verify a similar kind of current density peak at 400 °C. No voltammograms were recorded above 400 °C because of the thermal decomposition of NO_2 at higher temperatures [45]. Measurements on a portable flue gas analyzer (TESTO 350-S) show that ∼ 20% of the NO_2 have reacted into NO and O_2 at 400 °C, which has to be considered when the data are evaluated.

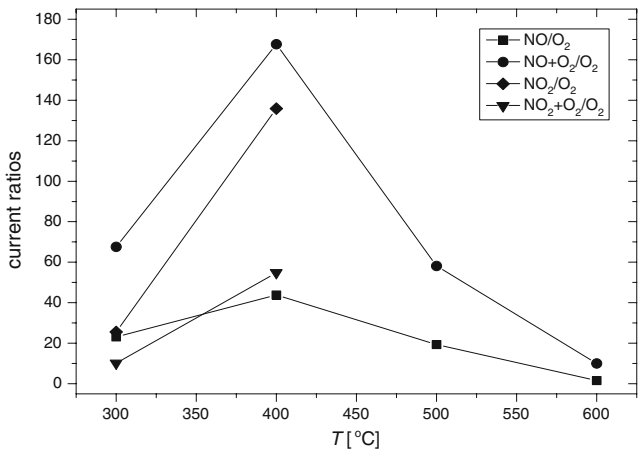

Fig. 10 Current ratios for the $MgFe_2O_4$ electrode measured as a function of temperature at −0.6 V

Figure 11 shows the theoretical calculations on the molar reaction as a function of OCV at 400 °C using Nernst Eq. 8:

$$E = \frac{-\Delta G^{\circ}}{nF} + \frac{RT}{nF} \ln K, \tag{8}$$

where ΔG° is the standard potential, n is the number of transferred electrons, F is the Faraday constant, R is gas constant, T is the temperature, and K is the molar reaction constant. An example of K for the reduction of NO to N_2 (Eq. 1) is shown in Eq. 9:

$$K = \frac{(1-\chi)^2}{\chi \cdot p_{O_2}/p^{\theta}}, \tag{9}$$

where χ is the molar reaction and p_{O_2}/p^{θ} is the partial pressure of oxygen in air divided with the standard pressure. The graphs show that the reduction of NO to N_2 lies at relatively high potentials, whereas the reduction of O_2 or NO_2 lies at potentials around −0.1 V. A suitable electrode material should therefore be able to reduce NO (or NO_2) without reducing O_2. Reactions involving N_2O are also shown; however, they are meant as a demonstration of how many processes can occur in the potential range.

The OCV of the different gas mixtures are shown in Fig. 12. The OCV of NO has much lower potentials compared to the thermodynamic calculations (Fig. 11) and it changes only very little as a function of temperature. The concentration gradient of O_2 over the electrolyte could increase the local oxygen partial pressure at the point electrode, which opens up for reactions

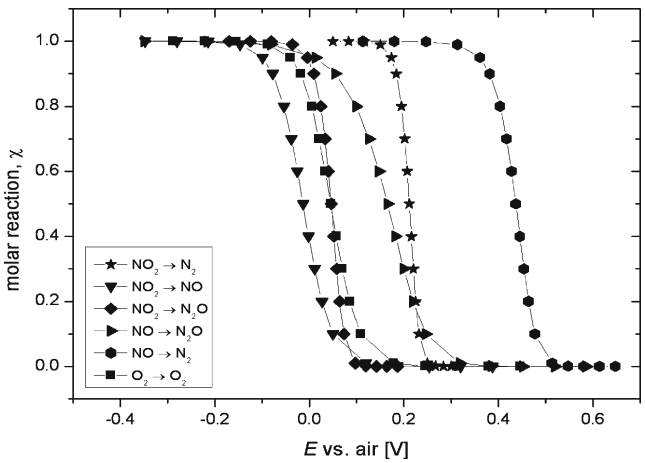

Fig. 11 Theoretical calculations on the molar reaction as function of OCV at 400 °C

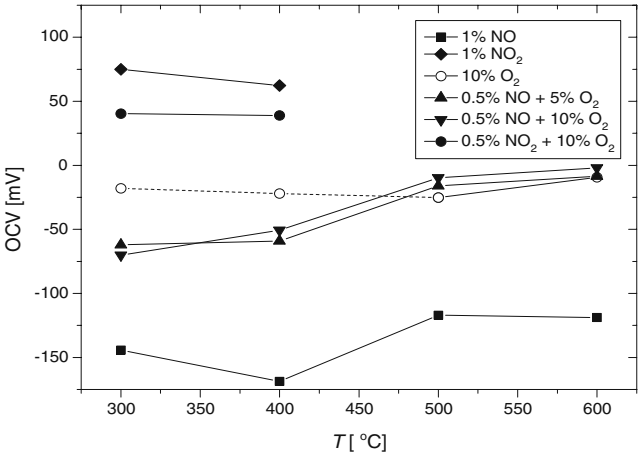

Fig. 12 OCV of $MgFe_2O_4$ in different gas mixtures as a function of temperatures. The *dotted line* of 10% O_2 from 300–400 °C shows the theoretical values of the standard potential

Eqs. 3 and 10 to occur. This and reaction kinetics will explain the lowering of the OCV.

$$O^{2-} + NO \rightarrow NO_2 + 2e^{-}. \tag{10}$$

The OCV of O_2 shows that the potentials at 500 and 600 °C are around −0.02 V, which is close to the standard potential calculated with FactSage 5.5. At 300 and 400 °C, OCV could not be measured with trustworthy accuracy. This is essentially a consequence of the shape of the CV curve, which has a wide region where the current is close to zero. This makes it difficult to measure the OCV since small fluctuations will have a great influence on recorded value. The presence of O_2 together with NO causes OCV to coincide with the OCV of O_2, suggesting that NO does not react at these potentials. The OCV of NO_2 and $NO_2 + O_2$ fall fairly close to each other, with $NO_2 + O_2$ at slightly lower potentials. The presence of O_2 and possible NO should decrease the OCV of $NO_2 + O_2$ according the measurements. However, OCV of $NO_2 + O_2$ still lies fairly close to the OCV of NO_2, suggesting a reaction involving NO_2 to be the dominant one.

Unfortunately, no direct gas conversion can be measured with the cone setup because of the low contact area of the point electrode and the relatively high flow rate. Therefore, we cannot supply a direct answer of the selectivity of the electrode material. However, it does supply information of the activity, which can be used as a relative tool to do further tests on those materials that exhibit high activity in different gases of interest. $MgFe_2O_4$ is considered a highly interesting candidate as a cathode material in electrochemical filters

for direct decomposition of NO_x gases. However, the recorded OCV implies that a relatively large over potential is needed in order to reduce NO on a $MgFe_2O_4$ electrode.

Conclusion

The electrochemical studies of Ni/Mg containing ferries with a spinel-type structure show that the two end members of the $NiFe_2O_4$–$MgFe_2O_4$ series have a relative high activity in NO in the measured temperature range. However, the activity in O_2 differs significantly from the two end members, with the $NiFe_2O_4$ electrode showing the largest activity. Recorded measurements on the $MgFe_2O_4$ electrode show that the current ratios of NO/O_2, $(NO + O_2)/O_2$, NO_2/O_2, and $(NO_2 + O_2)/O_2$ are much higher compared to the other spinels, with the exception of NO/O_2 at 600 °C. As more Fe^{3+} is incorporated on the octahedral site, the higher the conductivity is but the lower the activity in NO and O_2 is. Recordings of OCV suggest that the reduction of NO is inhibited by the presence of O_2, whereas the reduction of NO_2 seems to dominate in the presence of O_2. Four-point DC resistivity measurements show that $Ni_{0.5}Mg_{0.5}Fe_2O_4$ and $Ni_{0.4}Mg_{0.6}Fe_2O_4$ have the highest conductivity at elevated temperatures, whereas the spinels with low Mg content ($Ni_{0.7}Mg_{0.3}Fe_2O_4$ and $NiFe_2O_4$) have the highest conductivity at lower temperatures. An order–disorder of the cations could also be detected from the conductivity measurements in most of the samples. Measurement on thermal expansion show that the temperature of the magnetic order is detectable in all samples, but an additional wide peak is also detected in $MgFe_2O_4$ at 800 °C, which seems to be related to a cation reordering. Thermal expansion coefficients are comparable with CGO10, which is important since a composite electrode of spinel and CGO10 is needed in order to construct a usable electrode.

References

1. DieselNet (2008) www.dieselNet.com, Technical report
2. Pancharatnam S, Huggins RA, Mason DM (1975) J Electrochem Soc 122:869
3. Kammer K (2005) Appl Catal B 58:33
4. Gür T, Huggins R (1979) J Electrochem Soc 19:1067
5. Iwayama K, Wang X (1998) Appl Catal B 19:137
6. Hibino T (1995) J Appl Electrochem 25:203
7. Hibino T, Ushiki K, Kuwahara Y (1995) J Chem Soc Faraday Trans 91:1955
8. Hamamoto K, Fujishiro Y, Awano M (2007) J Electrochem Soc 154:F172
9. Hamamoto K, Fujishiro Y, Awano M (2006) J Electrochem Soc 153:D167
10. Changguan WF, Teraoka Y, Kagawa S (1996) Appl Catal B 8:217
11. Changguan WF, Teraoka Y, Kagawa S (1997) Appl Catal B 12:237
12. Shangguan WF, Teraoka Y, Kagawa S (1998) Appl Catal B 16:149
13. Haneda M, Kintaichi Y, Hamada H (2005) Appl Catal B 55:169–175
14. Drouet C, Alphonse P, Rousset A (2001) Appl Catal B 33:35
15. Simonsen VLE, Find D, Lilliedal M, Petersen R, Hansen KK (2007) Top Catal 45:143
16. Hansen KK, Christensen H, Skou EM (2000) Ionics 6:340
17. Chick LA, Pederson LR, Maupin GD, Bates JL, Thomas LE, Exarhos GJ (1990) Mater Lett 10:6
18. Koteswara Rao K, Banu T, Vithal M, Swamy GYSK, Ravi Kumar K (2002) Mater Lett 54:205
19. Petříček V, Dusek M, Palatinus L (2000) Jana2000, The crystallographic computing system. Institute of Physics, Praha
20. Hansen KK, Vels Hansen K (2007) Solid State Ionics 178:1379
21. Hansen KK (2007) Electrochem Commun 9:2721
22. Hansen KK, Christensen H, Skou EM, Skaarup SV (2000) J Appl Electrochem 30:193
23. Fabry P, Kleitz M, Deportes C (1972) J Solid State Chem 5:1
24. Newman J (1966) J Electrochem Soc 113:501
25. Appel CC, Bonanos N, Horsewell A, Linderoth S (2001) J Mater Sci 36:4493
26. Bruggerman DAG (1935) Ann Phys 24:636
27. Klein C, Hurlbut CS, Dana JD (1998) Manual of mineralogy, 21th edn. Wiley, New York
28. West AR (1987) Solid state chemistry and its applications, 2nd edn. Wiley, New York
29. Berchmans LJ, Kalai Selvan R, Selva Kumar PN, Augustin CO (2004) J Magn Magn Mater 279:103
30. Berchmans LJ, Kalai Selvan R, Augustin CO (2004) Mater Lett 58:1928
31. Ata-Allah SS, Fayek MK, Yehia M (2004) J Magn Magn Mater 279:411
32. Ata-Allah SS, Sayedamed FM, Kaiser M, Hashhash AM (2005) J Mater Sci 40:2923
33. Ziemniak SE, Anovitz LM, Castelli RA, Porter WD (2007) J Phys Chem Solids 68:10
34. Bozorth RM (1951) Ferromagnetism, 5th edn. D. Van Nostrand, New York
35. Harrison RJ, Putnis A (1999) Phys Chem Mineral 26:322
36. Turkin AI, Drebushchak VA (2004) J Cryst Growth 265: 165
37. Modi KB, Joshi HH, Kulkarni RG (1996) J Mater Sci 31:1311
38. Carter RE (1959) J Am Ceram Soc 42:324
39. Weil L (1951) J Phys Rad 12:260
40. Fagg DP, Kharton VV, Shaula A, Marozau IP, Frade JR (2005) Solid State Ionics 176:1723
41. Søgaard M, Hendriksen PV, Mogensen M (2007) J Solid State Chem 180:1489
42. Redfern SAT (2002) Eur J Mineral 14:251
43. Levy D, Diella V, Dapiaggi M, Sani A, Gemmi M, Pavese A (2004) Phys Chem Miner 31:122
44. Antao SM, Hassan I, Parise JB (2005) Am Mineral 90:219
45. ThermFact (2007) FactSage version 5.5. www.factsage.com
46. Bevan DJM, Shelton JP, Anderson JS (1948) J Chem Soc NOV:1729
47. Brabers VAM, Klerk J (1977) J Phys 38:207–209
48. Corbel G, Mestiri S, Lacorre P (2005) Solid State Sci 7:1216